The Astrophysical Journal, 877:148 (11pp), 2019 June 1 https://doi.org/10.3847/1538-4357/ab1b3b

Modeling the Effects of Observational Gaps on *p*-mode Oscillation Parameters

J. Z. Keith-Hardy[1,2], S. C. Tripathy[3], and K. Jain[3]
[1] National Solar Observatory REU Program, 3665 Discovery Drive, Boulder, CO 80303, USA; jzkeithh@colby.edu
[2] Physics Department, Colby College, Waterville, ME 04901, USA
[3] National Solar Observatory, 3665 Discovery Drive, Boulder, CO 80303, USA; stripathy@nso.edu, kjain@nso.edu
Received 2019 January 25; revised 2019 April 17; accepted 2019 April 19; published 2019 June 5

Abstract

We investigate the effect of the window function on the parameters of solar acoustic oscillations, namely frequency, amplitude, and width, using the data from Global Oscillation Network Group (GONG). This is carried out by simulating 108 new time series from a base time series by modifying the window functions. In order to minimize the effect of solar activity, the base time series was chosen during the activity minimum period. The new window functions were randomly chosen from a set of 30 observed window functions to incorporate the reported duty cycles of the GONG network. The modified time series were processed through the standard GONG *p*-mode pipeline to extract the mode parameters that were fitted to a linear model as a function of the duty cycle to yield the correction factor. We find significant changes between the observed and corrected amplitudes and widths while the change in mode frequencies was found to be insignificant. We also analyze the variation of the corrected mode parameters over the solar cycles 23 and 24 and compare their correlations with 10.7 cm radio flux, which represents a proxy of the solar activity.

Key words: Sun: activity – Sun: helioseismology – Sun: interior – Sun: oscillations

1. Introduction

The oscillation frequencies of the Sun have been widely used in helioseismic studies to infer the internal structure and dynamics of the Sun. In addition, mode amplitudes and widths have also been used to infer the energy and rate of change of energy throughout the solar cycle. Therefore, accurate estimation of these mode parameters is an important step in the helioseismic data reduction procedure. However, helioseismic observations carried out from both the ground- and space-based observatories are often complicated due to the absence of data in some time interval; the problem is more severe in ground-based observations. In order to minimize such gaps, the Global Oscillation Network Group (GONG; Harvey et al. 1996) observes the Sun from six stations around the world. Nevertheless, instrument breakdowns and poor weather conditions still cause interruptions (Hill et al. 1988). Gaps in observations lead to aliasing in the frequency domain and create spurious side lobes that lead to ambiguous identification of real frequencies and other mode parameters.

Deconvolution methods have been suggested to remove the effects of gaps. Techniques for estimating better power spectra from time series with gaps were developed in the 1980s and early 1990s but are generally applied to data with short gaps. Fahlman & Ulrych (1982) used a maximum-entropy reconstruction method to estimate the power and phase spectra of gapped time series. Brown & Christensen-Dalsgaard (1990) modified this technique for solar oscillation data and concluded that the method provides good results if the signal-to-noise ratio in the original data is large enough and the gaps are short. Lazrek & Hill (1993) examined the effects of gaps by simulating observations of a single spectral line convolved with a window function. Using a maximum-likelihood technique, the authors found that the central frequency, mode amplitudes, and widths are slightly sensitive to the duty cycle as long as the gaps occur frequently and are short. However, this simulation was performed on a single isolated spectral line with no nearby peaks, which is different from a real solar spectrum. Using simulated data, Chang & Gough (1995) also tried to remove the effect of data gaps by fitting the temporal signal to a model produced by the superposition of many modes, rather than using its power spectrum. This analysis is of limited use because it is based on simplified assumptions. A more detailed analysis of the impact of the duty cycle on the measurement of low-degree oscillation-mode frequencies was carried out by simulating different combinations of window functions and numbers of observing stations (Chaplin et al. 2003, 2004; Broomhall et al. 2015). These studies concluded that for the majority of the low-degree modes the bias in the frequencies given by the effects of the window function is not significant. In the realm of intermediate-degree modes, few studies have been carried out to correct the mode parameters by assuming a linear relationship between these and a combination of magnetic field with duty cycle (Komm et al. 2000; Tripathy et al. 2006; Kiefer et al. 2018). However, a better approach would be to follow the procedure outlined in Chaplin et al. (2004) and create several time-series data where the effect of the duty cycle is simulated by changing the window function of a base set to estimate the mode parameters. Thus, any deviation in the mode parameters will be only due to the changes in duty cycle. In this paper, we follow this procedure and for the first time investigate the influence of the duty cycle on intermediate-degree mode frequencies, amplitudes, and widths using simulated data sets with different duty cycles. We also examine the temporal variations of corrected mode parameters as a function of the solar activity level as measured by the 10.7 cm radio flux ($F_{10.7}$), and compare these results with the uncorrected mode parameters.

2. Construction of Simulated Data Sets

As a standard data product, the GONG network generates time series that span a period of 36 days and are referred to as one GONG Month (GM). However, to improve the signal-to-noise ratio and to obtain a better frequency resolution, the mode parameters are computed from a time series of 108 days spaced

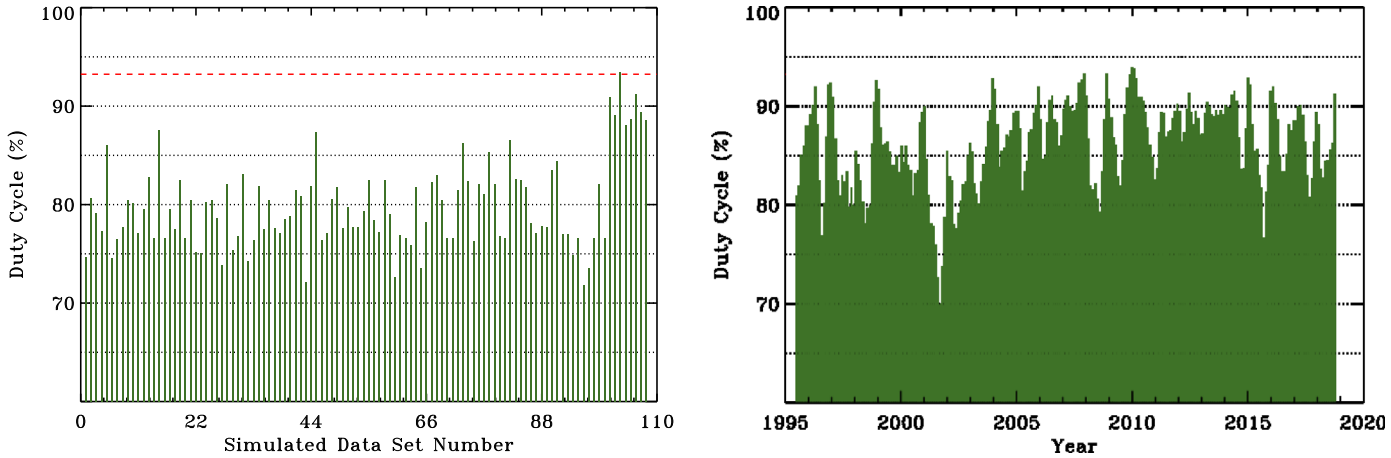

Figure 1. Duty cycles of the 108 sets of simulated data (left panel) compared to duty cycles of 237 GONG months covering the period of 1995 May 7 to 2018 November 25 (right panel). The dashed red line in the left panel denotes the duty cycle of the base data set used in simulating the 108 new time series.

by 36 days, i.e., each series is overlapped by 72 days. Each time series that comes from the GONG data contains a window function, $w(t)$, that follows the following two state formula:

$$w(t) = \begin{cases} 0 & \text{for } v(t) = 0 \\ 1 & \text{for } v(t) \neq 0 \end{cases} \quad (1)$$

where $v(t)$ represents the status of the observation and has a value of 1 if data are usable or 0 otherwise. The aggregate of non-zero window function is defined as the duty cycle, D, which is generally expressed as a percentage. In the case of the GONG data, each t described in Equation (1) represents a minute's worth of data. The duty cycles of 237 data sets used in this study vary between 70% and 94% and are shown in Figure 1.

In general, the variation in mode parameters can be ascribed to the changes in solar activity and the duty cycle (Komm et al. 2000). However, we are interested in analyzing the effect of the duty cycle only, therefore we minimize the effect of the activity by choosing the base data set during the activity minimum period between solar cycles 23 and 24. Based on the solar activity measured by 10.7 cm radio flux, we select the period of 2008 October 1 to 2009 January 16 (corresponding to GM 137–139) during which the daily flux values varied between 65.2 and 71.4 sfu with a mean value of 67.3 sfu over 108 days. Thus, GMs 137–139 centered on 2008 November 23 with a fractional duty cycle value of 0.93 (shown as a dashed line in the left panel of Figure 1) constitute the base time series. For this study, we simulate a total of 108 independent time series by changing the window function of the base set following the method similar to that described in Chaplin et al. (2004). To do this, we first choose 30 different GMs (listed in Table 1) with duty cycles varying between 71% and 94% and then concatenate 3 randomly chosen window functions to generate 108 new window functions that are 108 days long. We then multiplied the window function of the base series, $v(t)$, by each of the 108 combinations to obtain 108 new window functions, $w_i'(t)$, whose duty cycle values varied between 71.9% and 93.4%. These values are plotted in the left panel of Figure 1. Examples of the distribution of the gap lengths binned over a 1 hr time interval for the base time series and a time series with a fractional duty cycle value of 0.80 are compared in Figure 2. For the base time series with a high value of duty cycle, most of the gaps are short in nature, while for the low duty cycle series, the gaps could be as large as 15 hr each. In general, we find that the short gaps (between 1 and 60 minutes) occur most of the time, while gap lengths of longer duration occur a few times when the time series has a low duty cycle.

Table 1
Duty Cycles of Selected GONG Data to Simulate 108 Sets of Random Window Functions with Varying Duty Cycles

Set Number	Period		GONG Month GM	Duty Cycle
	Start	End		
1	1995 May 7	1995 Jun 11	1	0.783
2	1996 Jul 12	1996 Aug 16	13	0.729
3	1997 Mar 21	1997 Apr 25	20	0.793
4	1997 Oct 23	1997 Nov 27	26	0.748
5	1998 Jul 2	1998 Aug 6	33	0.724
6	2001 Feb 28	2001 Apr 4	60	0.768
7	2001 May 11	2001 Jun 15	62	0.779
8	2001 Jun 16	2001 Jul 21	63	0.759
9	2001 Aug 27	2001 Oct 1	65	0.680
10	2001 Oct 2	2001 Nov 6	66	0.676
11	2003 Mar 26	2003 Apr 30	81	0.765
12	2004 Apr 25	2004 May 30	92	0.833
13	2005 Apr 20	2005 May 25	102	0.746
14	2008 Jan 23	2008 Feb 27	130	0.880
15	2008 Feb 28	2008 Apr 3	131	0.782
16	2008 Apr 4	2008 May 9	132	0.803
17	2008 May 10	2008 Jun 14	133	0.862
18	2008 Jun 15	2008 Jul 20	134	0.799
19	2008 Jul 21	2008 Aug 25	135	0.773
20	2008 Aug 26	2008 Sep 30	136	0.804
21	2008 Oct 1	2008 Nov 5	137	0.924
22	2008 Nov 6	2008 Dec 11	138	0.930
23	2008 Dec 12	2009 Jan 16	139	0.943
24	2009 Jan 17	2009 Feb 21	140	0.848
25	2009 Feb 22	2009 Mar 29	141	0.874
26	2009 Mar 30	2009 May 4	142	0.881
27	2009 May 5	2009 Jun 9	143	0.826
28	2009 Jun 10	2009 Jul 15	144	0.779
29	2009 Jul 16	2009 Aug 20	145	0.853
30	2015 Oct 1	2015 Nov 5	208	0.709

Note. Columns 2 and 3 specifiy the start and end of the GONG month, while column 4 denotes the corresponding GONG month that corresponds to 36 days. The last column shows the fractional duty cycle.

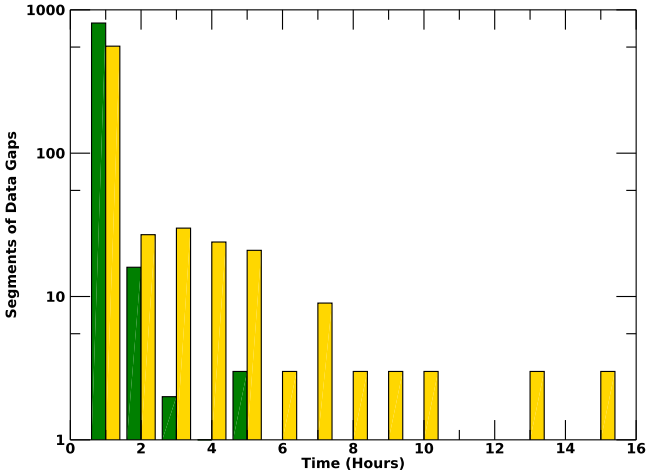

Figure 2. Distribution of gaps for two different time series is shown by binning the number of gaps over a 1 hr time interval. The green bars represent the base time-series data with a duty cycle of 93.3%, while the yellow bars represent the time series with a low duty cycle of 80%.

These new simulated window functions representing data gaps, which are derived from real observations, were then used with the base time series to create 108 new time series using the following equation:

$$v_i'(t) = v(t) * w_i'(t). \quad (2)$$

These were subsequently processed through the standard GONG pipeline, which computes power spectra based on the multi-taper spectral analysis (Komm et al. 1999) and fits a Lorentzian profile to fit all peaks, both target and spatial leaks, in the $m - \nu$ spectrum using a minimization scheme described in Anderson et al. (1990). More details on the procedure can be found in Hill et al. (1998) and Jain et al. (2011). The final output tables return frequency $\nu_{n\ell m}$, amplitude $A_{n\ell m}$, width $\Gamma_{n\ell m}$, two background parameters, and their associated errors for each n, ℓ, m mode in an n, ℓ multiplet where n is the radial order, ℓ is the harmonic degree, and m is the azimuthal order with a value of $-\ell \leqslant m \leqslant \ell$. Each table computed from 108 day long time series contains more than 350,000 modes for ℓ in the range of 0–150. However, in this analysis we will only focus on m-averaged mode parameters, i.e., for each n, ℓ value, we average each parameter over all fitted m values, which are considered to be "good modes," as indicated by the error flags in the GONG peak fitting algorithm (Hill et al. 1998). We further restrict our analysis to frequencies in the range 1500–4500 μHz, where the modes have a sufficiently large signal-to-noise ratio and are adequately resolved from the neighboring leaks.

As an example of variation of the mode parameters, Figure 3 shows the mode power as a function of the frequency for three different values of the duty cycle in a limited frequency range. The black line is the power spectrum of the base set ($D = 93.3\%$). The red and blue lines represent the power spectra corresponding to the modified time series with duty cycles of 71.9% and 82%, respectively. It is clear that the mode power decreases as the duty cycle decreases. A more detailed analysis of the variation of mode amplitude is described later.

In addition to these mode parameters, we also use central frequencies, ν_{nl}, which are estimated by fitting a Legendre polynomial series to the multiplet frequencies:

$$\nu_{nl} = \nu_{nlm} - \sum_{j=1}^{j} a_j(n, l)P_j(m/l), \quad (3)$$

where P_j is the jth order Legendre polynomial, and a_j are the splitting coefficients (the file names are tagged as "mrv1z"). In addition to the m-averaged mode parameters, we also investigate the variation of the central frequencies.

3. Dependence of Mode Parameters on Duty Cycle

Figure 4 shows the number of modes present in central frequency tables in the ℓ range between 0 and 150. It reveals that the total number of fitted modes is a random value and does not increase monotonically with the increase of the duty cycle. For example, with a fractional duty cycle of 0.80, the number of modes fitted is larger by approximately 3% than those fitted from the base set. A similar result is found when the local helioseismic data from Helioseismic Magnetic Imager (HMI) was analyzed in a similar procedure (Tripathy et al. 2018). We assume that the computed mode parameters from simulated sets are independent of magnetic activity and are affected only by the duty cycle, because the simulated time series are derived from the base time series during the activity minimum period. Following Chaplin et al. (2004), we assume that the mode parameters are linearly dependent on the duty cycle and the m-averaged parameters are then regressed linearly against the duty cycle, e.g., for frequencies

$$\delta\nu_{nl\overline{m}} = a_{nl} + b_{nl}(100 - D), \quad (4)$$

where $\delta\nu_{nl\overline{m}}$ is the frequency difference with respect to the base set, a_{nl} and b_{nl} are the best-fitting intercept and gradient, respectively. The choice of the factor, $100 - D$, ensures that the intercept is zero, corresponding to the frequency expected when $D = 100$. Therefore, one can fit Equation (4) without the intercept term, using the frequency differences instead of the actual frequencies as rendered in Komm et al. (2000) and Chaplin et al. (2004). However, the variations in the width, as well as the amplitude, are larger than frequency and hence a linear fit between the difference value and D will not provide any meaningful gradient values. Therefore, for these two parameters, we chose to normalize with the value from the base set, so that the intercept has a value of 1 when $D = 100$. Note that henceforth we will be working with difference and ratio terms, therefore the fitted parameters from the base set will be referred to as the reference set.

3.1. Frequency Differences

Figure 5 shows the difference for the $n = 10$ and $\ell = 55$ modes between the 108 simulated and reference frequencies as a function of the duty cycle as $100 - D$. The solid line in Figure 5 demonstrates the linear fit and indicates a frequency difference of about 0.25 μHz or about 0.008% of the reference value at a duty cycle of 70%. This calculation was repeated for all "good modes," i.e., modes that appeared in at least 66% out of the 108 sets. The resultant gradients as a function of frequency are presented in Figure 6. The dashed line in the figure represents the 3σ deviation from the median value. Mostly, the gradient is well within 3σ values except near the high end of the frequencies ($\nu > 4000\ \mu$Hz) where the fitting

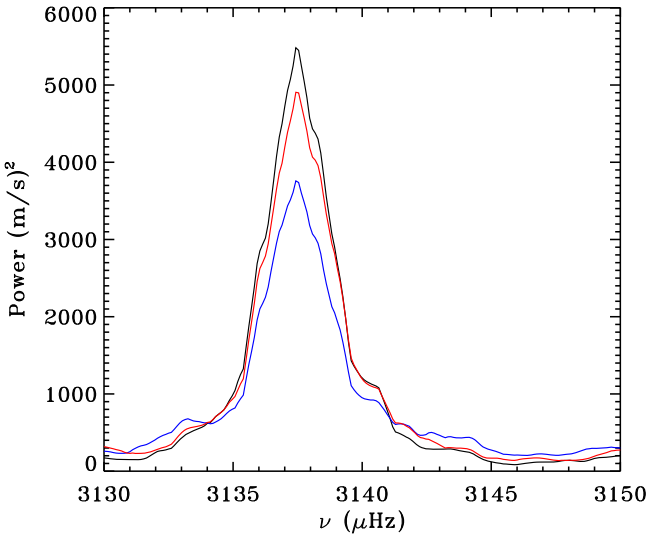

Figure 3. Examples of the power spectrum for the $n = 10$ and $\ell = 55$ mode. The black line is the power spectrum of the base set. The red and blue lines represent the power spectra corresponding to the simulated time series with duty cycles of 82% and 71.9%, respectively.

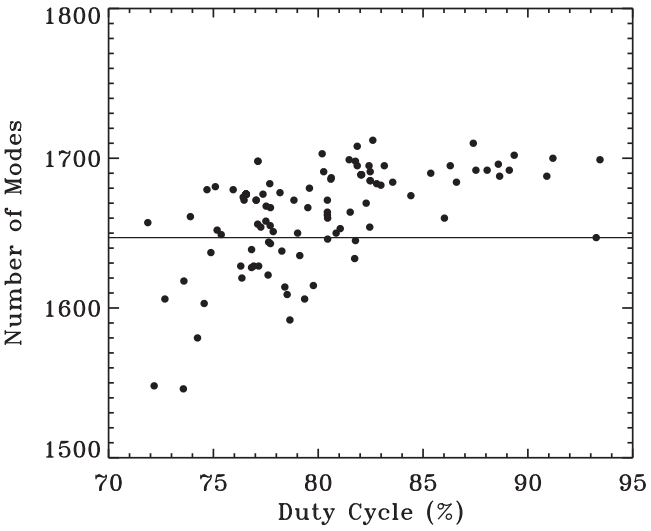

Figure 4. Number of fitted modes from each of the 108 simulated time series. The number is counted from central frequency, ν_{nl}, tables. The solid line is the value corresponding to the base time series.

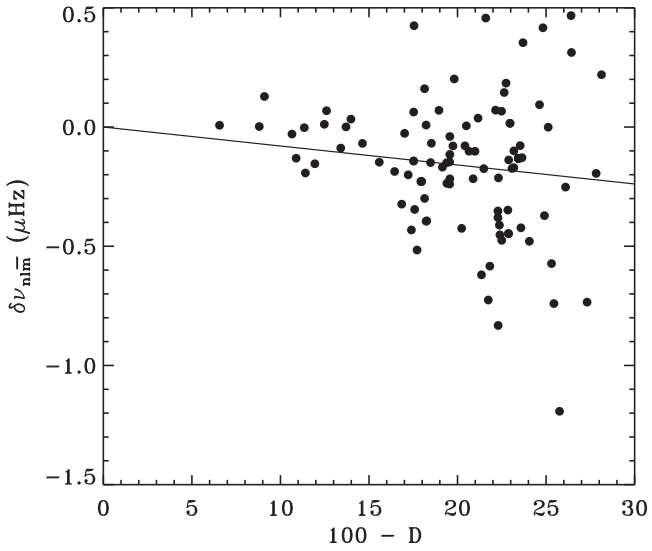

Figure 5. m-averaged frequency differences between 108 sets of simulated data and the reference value as a function of the duty cycle (expressed as percentage) for the $n = 10$ and $\ell = 55$ mode. The solid line is the best fit between the two, obtained assuming an intercept of zero at a 100% duty cycle. For this mode, the reference value is 3137.5144 μHz and the gradient is -7.961×10^{-3} μHz.

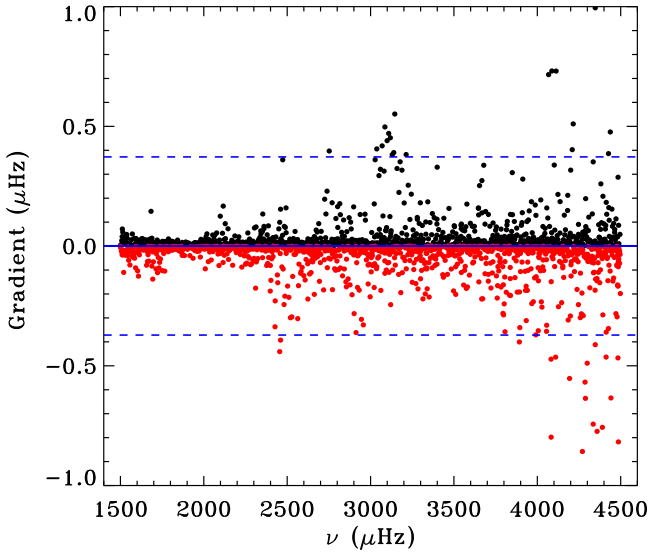

Figure 6. Computed gradients for all m-averaged frequencies between 1500 and 4500 μHz. The black and red points denote positive and negative gradients. The solid line represents the median value, while the dashed line represents 3σ deviation from the median value.

uncertainties are higher, which suggests a high scatter in frequency differences. We also note that the gradient is both positive and negative, with approximately 51% of the modes having a positive gradient (black points) and 49% having a negative gradient (red points) across the frequency range considered. Thus, there is no clear bias in the data and the sign of the gradient depends on the multiplet considered. In the context of the low-degree modes, Chaplin et al. (2004) also found a similar result, i.e., the gradients were found to be both positive and negative depending on the radial order of the mode.

The calculation of the gradients for ν_{nl} was repeated following the same procedure as $\delta\nu_{nl\bar{m}}$. Figure 7 shows the difference for the same mode ($n = 10$ and $\ell = 55$) and the solid line represents the linear fit with a χ^2 value of less than 10^{-10}. However, in this case, the frequency differences are smaller by a factor of 10 compared to the m-averaged frequency differences. Furthermore, we computed the gradients of modes common in all data sets and both positive (black points) and negative (red points) are displayed in Figure 8 with a distribution percentage of 71.3% and 28.7%, respectively. Similar to the m-averaged frequencies, we do not find any significant bias as a function of the frequency, but the number of modes with positive gradients is significantly higher than the number of modes with negative gradients. We also note that most of the gradients are confined within 1σ of the median value and few deviations are noted only at higher frequencies. We further note that the values of the gradients are rather small and have a median value of 0.406 nHz, signaling that the effects of the duty cycle on the central frequencies may not be significant.

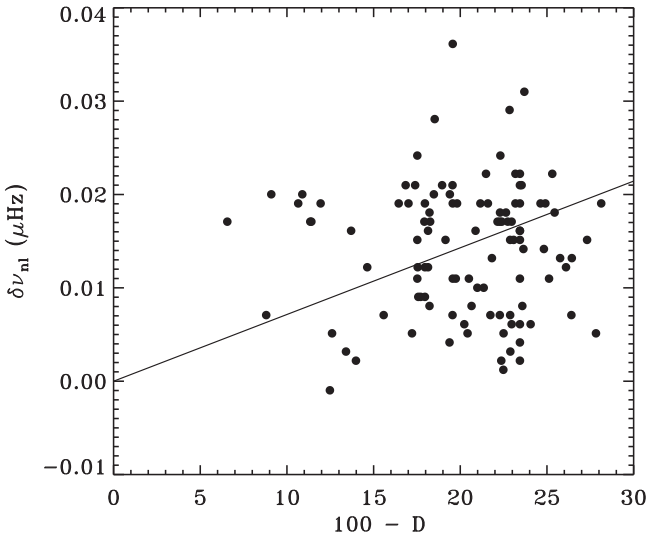

Figure 7. Same as Figure 5 but for central frequencies, ν_{nl}. The reference value is 3137.5149 μHz. The gradient for this mode is 7.145 $\times$ 10^{-4} μHz.

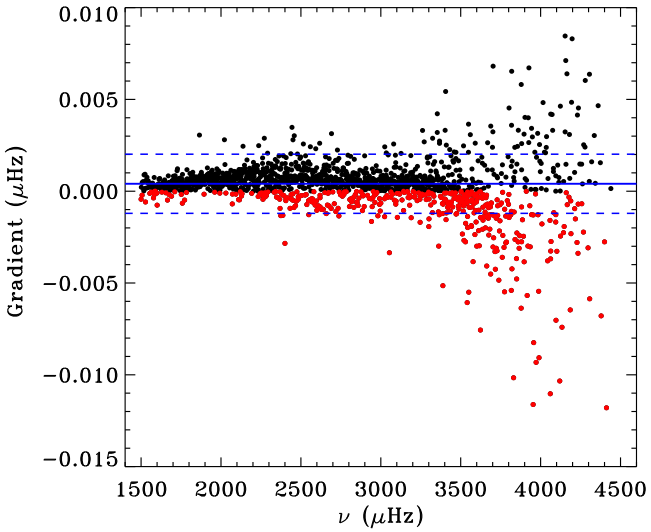

Figure 8. Same as Figure 6 but for central frequencies, ν_{nl}. The solid line represents the median value, while the dashed line represents a 1σ deviation from the median value.

3.2. Mode Amplitude and Width

Figure 9 shows the linear dependence between the normalized width (bottom panel) and amplitude (top panel) and duty cycle for the $n = 10$ and $\ell = 55$ mode. However, it appears that the normalized amplitudes display a systematic curve instead of a linear trend. Thus, we refitted the amplitudes (and widths) with a quadratic relation ($\delta A_{nl\bar{m}} = \alpha_{nl} + \beta_{nl}(100 - D) + \gamma_{nl}(100 - D)^2$), where δA is the amplitude ratio with respect to the reference set and α_{nl} has a value of 1 when $D = 100$. In each panel, the resultant quadratic fit is shown as a dashed line. Clearly, for the mode widths, there is no significant difference between the two fitted curves, while the amplitude around the low duty cycle values demonstrates a marginally better fit when the quadratic relation is used. The fitted coefficients for both linear and quadratic fits are presented in Table 2. It is evident that the second order coefficients for both amplitude and width are smaller by a factor of about 10^{-2} compared to the first-order coefficients. Therefore we assume that the variations of amplitudes and widths are linear and use the gradients from the linear fit to correct the mode amplitudes and widths.

Since a higher duty cycle suggests a better determination of the line profiles, we expect that the mode width should decrease and amplitude should increase with the duty cycle. This implies that the gradients of the width and amplitude should display the opposite behavior. This is what we see in Figure 9: a decreasing trend for the widths and increasing trend for the mode amplitudes with the increase of the duty cycle.

In order to analyze the distribution of the gradients of all m-averaged amplitudes and widths, we plot these as a function of frequency in Figure 10. In the case of widths, we find that the gradients are mostly positive (86.2%) and peak around 3000 μHz range, while the negative gradients are confined to the low and high ends of the frequency distribution. In a similar way, the gradients corresponding to normalized amplitude values are mostly negative (99.7%) and the maximum distribution occurs around the same range as the width. This further implies that in the 3000 μHz range, the mode widths and amplitudes are significantly affected by the duty cycle and would result in a significant correction to the observed quantities. In order to determine, the ℓ range, where the correction would be most significant, we plot the gradients as a function of the degree of the mode (Figure 11) and it is clear that significant changes would occur for ℓ values approximately between 30 and 80.

4. Solar Cycle Variation of Mode Parameters

It is now well established that the mode parameters vary with the Sun's magnetic cycle. However, in the case of oscillation frequencies, which have been studied extensively by many authors (e.g., Jain et al. 2009; Simoniello et al. 2013; Broomhall & Nakariakov 2015; Salabert et al. 2015; Tripathy et al. 2015; Howe et al. 2018), a few interesting results were obtained during the extended minimum period between solar cycles 23 and 24. For example, the analysis of frequencies of low-degree modes from the Global Oscillations at Low frequency (GOLF) instrument pointed out that cycle 24 started in 2007 (Salabert et al. 2009), which was not confirmed by the analysis of intermediate-degree modes (Tripathy et al. 2010). Later, Jain et al. (2011) pointed out the existence of two minima in oscillation frequencies depending on the lower turning point radius of the propagating wave. In the context of other mode parameters viz. mode amplitudes and widths of intermediate degrees, limited investigations have been carried out. Using GONG data between 1995 and 1998, Komm et al. (2000) reported an increase in width and decrease in mode amplitude and mode area. Tripathy et al. (2006) compared mode parameters obtained from time series of different lengths using data from GONG and Michelson Doppler Imager (MDI) over a period of more than 10 yr and concluded that the mode amplitude and area clearly manifest anti-correlation, while the background amplitude and width averaged over all the multiplets are not correlated with solar activity cycle, although widths of single modes indicated marginal correlation. Thus, the nature of the correlation between width and solar activity differed between our analysis and those of Komm et al. (2000). In a recent study, Kiefer et al. (2018) followed the earlier work of Komm et al. (2000) to extend the analysis up to the period of 2017 June 3 (GM 223) and suggested that the level of correlation between mode parameters and solar activity depends on the mode frequency and harmonic degree. Thus,

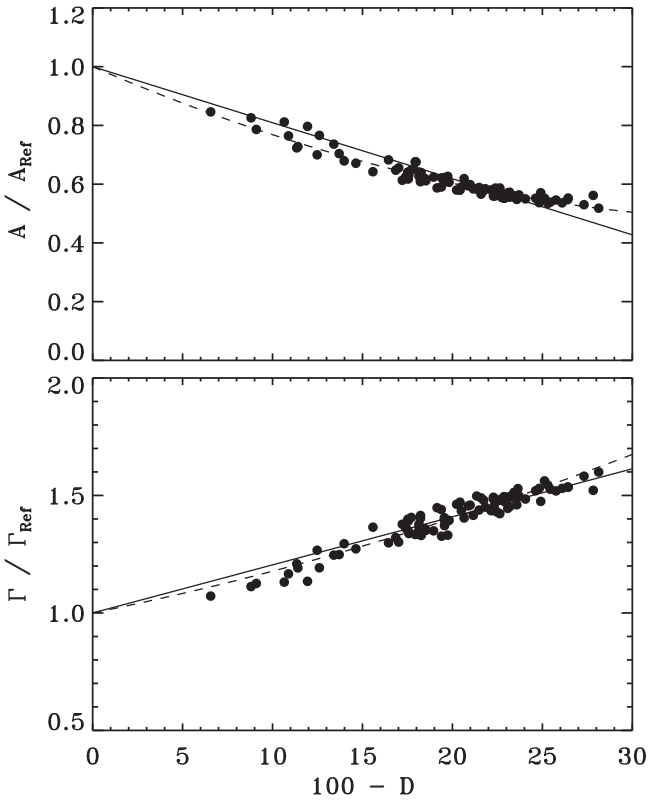

Figure 9. Normalized width, Γ, (bottom panel) and amplitude, A, (top panel) between 108 sets of simulated data and base set as a function of the duty cycle (expressed as percentage) for the $n = 10$ and $\ell = 55$ mode. The solid and dashed lines are the best linear and quadratic fits assuming an intercept of 1 at a 100% duty cycle. The reference values are 1.5113 μHz for width and 14375.24 $(\mathrm{m/s})^2$ for amplitude.

Table 2
Fitting Coefficients for Amplitude and Width for the $n = 10$ and $\ell = 55$ Mode

Mode Parameter	Linear Fit	Quadratic Fit	
	β_{nl}	β_{nl}	γ_{nl}
Amplitude ($(\mathrm{m/s})^2$)	−0.019086	−0.026488	0.000332
Width (μHz)	0.020453	0.015406	0.000236

Note. For each parameter, α_{nl} has a value of 1 at $D = 100$.

to comprehend the response of the corrected mode parameters to the solar activity over a period of 22 yr, we examine their temporal variation and analyze their relation to solar activity using the $F_{10.7}$ as the activity indicator.

4.1. Mode Frequencies

Equipped with the gradients for each m-averaged multiplet, we proceeded to correct the mode parameters for the standard GONG data consisting of 237 data sets covering the period of 1995 May 7 through 2018 November 25 following the linear relation:

$$\delta\nu_c(nl\overline{m}) = \delta\nu(nl\overline{m}) - a_{nl}(100 - D), \quad (5)$$

where $\delta\nu_c(nl\overline{m})$ is the difference between the corrected frequencies (frequencies at 100% duty cycle) with respect to

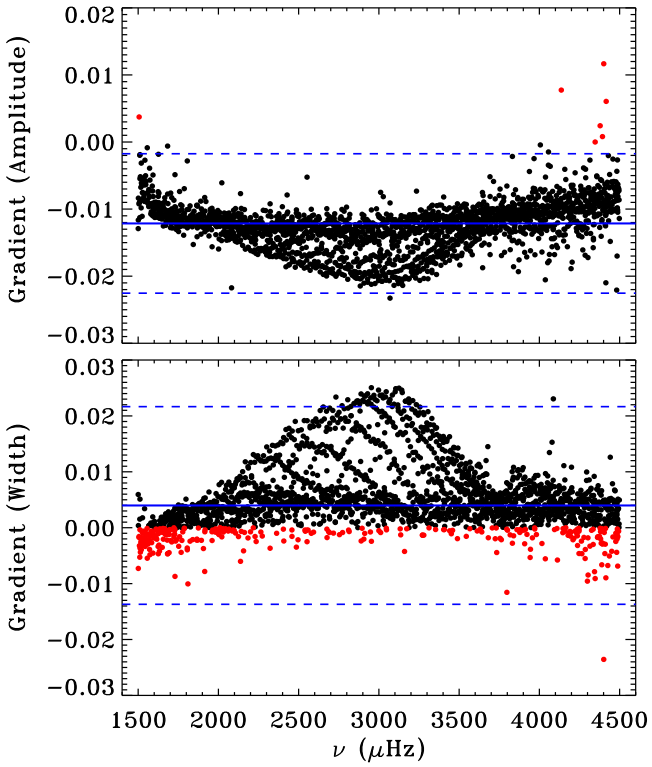

Figure 10. Slopes corresponding to normalized width (bottom panel) and amplitude (top panel) for all modes as a function of the frequency of the mode. The solid line represents the median value, while the dashed line represents a 3σ deviation from the median value.

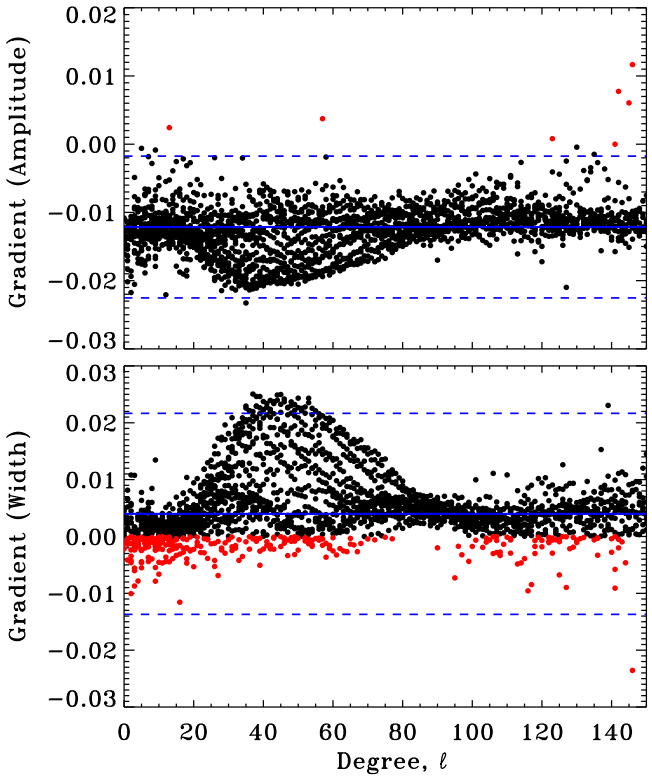

Figure 11. Same as Figure 10 but as a function of the degree of the mode.

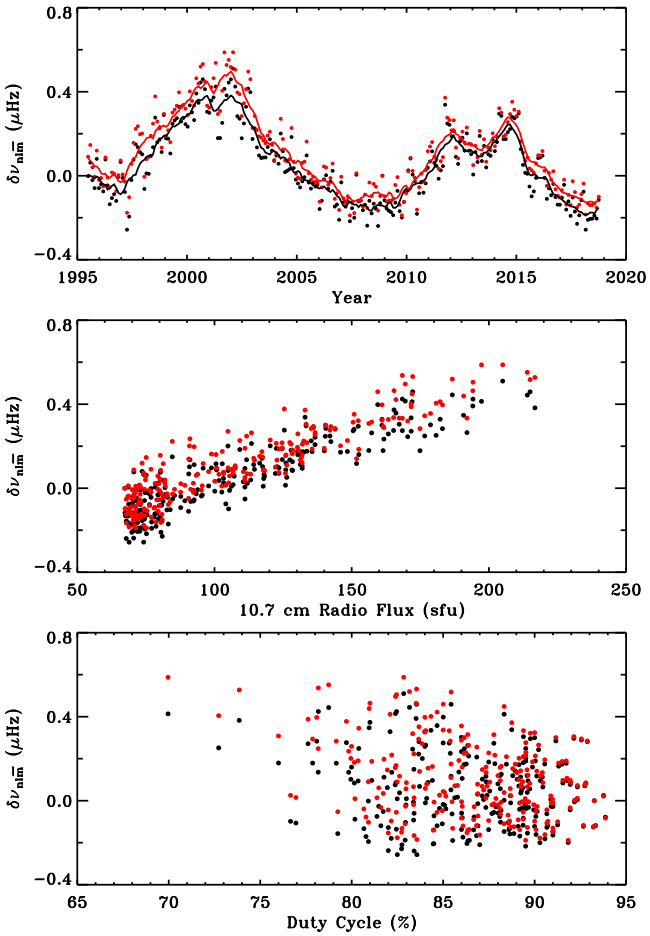

Figure 12. *m*-averaged mean frequency shifts averaged all modes common in the 237 data sets. The points shown in red represent the mean of the corrected values for each data set, while the black points denote the mean of the uncorrected values. The corrected shifts are obtained by subtracting the corrected reference values. The lines in the top panel represent the 1 yr boxcar-smoothed values and depict the solar cycle.

the corrected reference set (for A and Γ this would be ratio instead of difference). Finally, we take the mean over the common multiplets in each GONG month and plot them as a function of the duty cycle in bottom panel of Figure 12. As expected, the correction produced a minimal change in mode frequencies with a median difference of 40 nHz between the two. We further display the mean frequency differences as a function of $F_{10.7}$ (middle panel) and measure their association by computing the Spearman's rank correlation, ρ, which is found to be 0.91 and 0.88 for uncorrected and corrected frequencies, respectively. This further confirms that the frequencies are marginally dependent on the duty cycle. The top panel of Figure 12 illustrates the temporal evolution of the mean frequency differences. The smoothed shifts are connected to depict the solar cycle, where the smoothing is performed over a period of approximately one year. It may be noted that the apparent differences between the corrected (red line) and uncorrected (black line) mean frequency shifts are due to subtraction of different mean values. In addition to the *m*-averaged frequencies, we also corrected the central frequencies and computed the error-weighted mean frequency difference

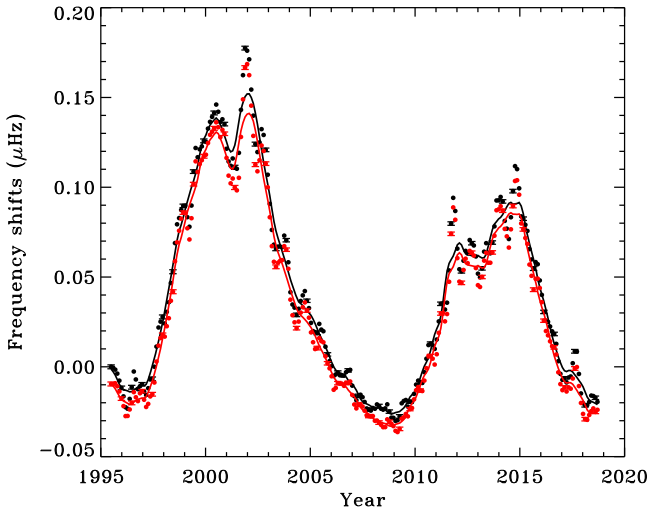

Figure 13. Error-weighted frequency shifts, $\delta\nu$, calculated using Equation (6) and central frequencies, ν_{nl}. The red points represents the shifts that are obtained after the frequencies are corrected for the effect of the duty cycle. The black points denote the shifts corresponding to the original values. The lines represent the 1 yr boxcar-smoothed values and illustrate the solar cycle.

using the standard relation

$$\delta\nu(t) = \sum_{n,l} \frac{Q_{nl}}{\sigma_{nl}^2} \delta\nu_{nl}(t) / \sum_{n,l} \frac{Q_{nl}}{\sigma_{nl}^2}, \quad (6)$$

where Q_{nl} is the mode inertia ratio, σ_{nl} is the error in frequency measurement, and $\delta\nu_{nl}(t)$ is the change in measured frequency for a given n, l pair. Figure 13 displays both the corrected (red line) and uncorrected (black line) $\delta\nu$ and no discernible difference can be seen between the two lines; the maximum difference is 1.7 nHz, which is about 100 times smaller than the measured fitting uncertainty. Once again, we measure the Spearman's rank correlation between $\delta\nu$ and $F_{10.7}$ and find ρ to be approximately 0.99, indicating a significant correlation with solar activity as has been noted in many earlier studies (Jain et al. 2011, and references therein)

4.2. Mode Amplitudes and Widths

Figure 14 shows both the corrected and uncorrected, *m*-averaged mean amplitudes and widths where the mean is taken over all n, ℓ modes (1902) that are common in all 237 data sets. As expected, the duty cycle correction decreases the width and increases the amplitude, corroborating the result of Kiefer et al. (2018). The top panel of Figure 14 shows the temporal variation of these parameters, where the solid lines represent smoothed values over a period of approximately one year and illustrate the solar cycle variation. The mean change between the corrected and uncorrected mean amplitudes and widths are about 10% and 3%, respectively, with the largest changes observed during 2001–2002, when the solar activity is higher. As found in earlier studies of low-degree modes, (Broomhall et al. 2015, and references therein), the widths are higher at solar maximum, suggesting that the modes are heavily damped during higher activity periods, while the decrease of amplitudes during the same period implies lower excitation. We further assess the correlation between these mean values and $F_{10.7}$ and confirm earlier findings that the mode amplitudes are anti-correlated, while widths are correlated with the $F_{10.7}$ activity

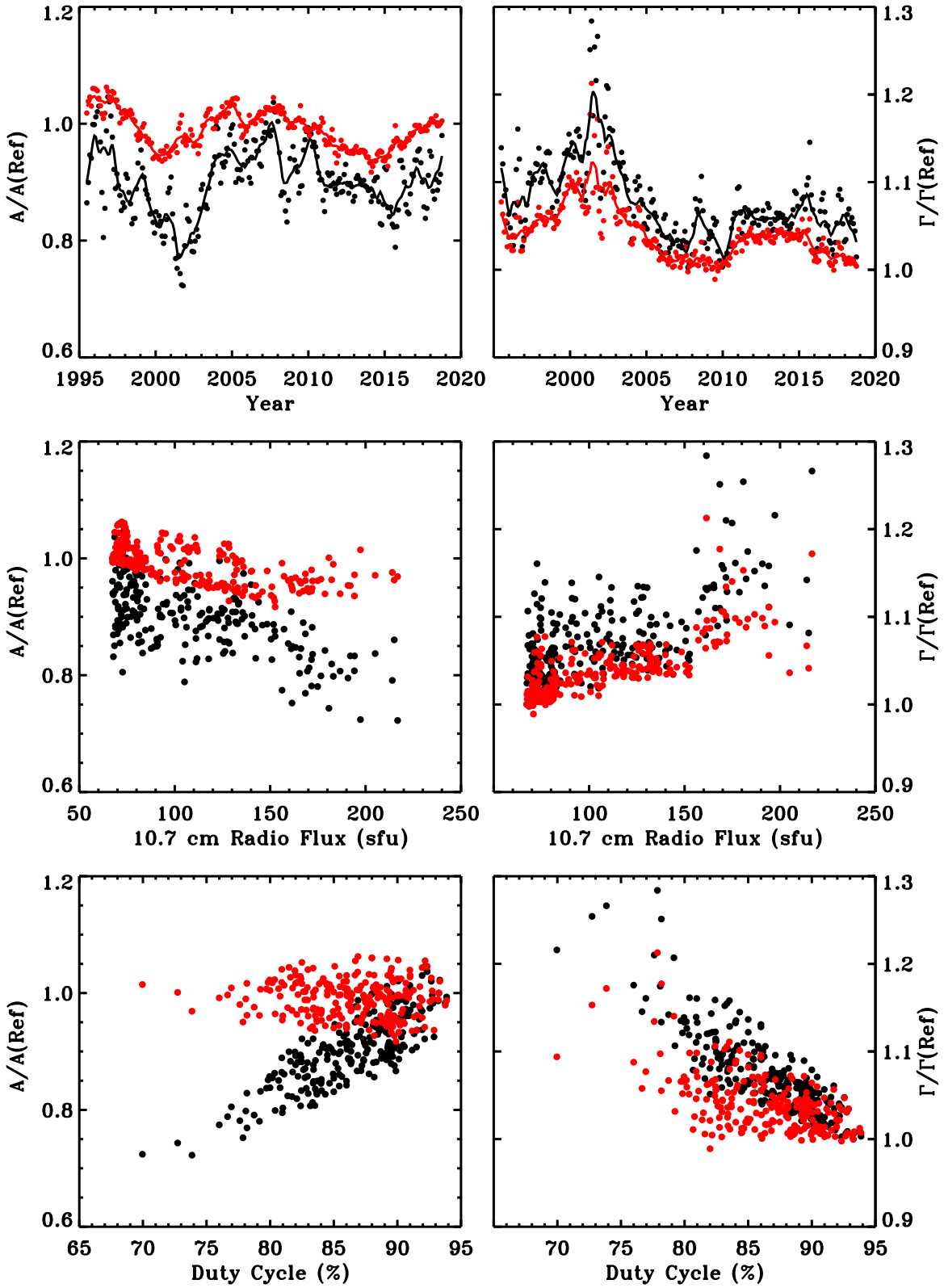

Figure 14. *m*-averaged mean amplitudes and widths averaged over all modes common in 237 data sets. The points shown in red represent the mean of the corrected values for each data set, while the black points denote the mean of the uncorrected values. The corrected ratios are normalized with the corrected reference values. The lines in the top panels represent the 1 yr boxcar-smoothed values and illustrate the solar cycle.

proxy. Importantly, we note that ρ changes by 25% and 13% between the corrected and uncorrected values for mode widths and amplitudes, respectively, indicating a significant change for the widths as compared to the amplitudes.

Kiefer et al. (2018) reported jumps in the mode amplitudes around GM 60 (2001 March) and 100 (2005 February), where the former refers to the period when the cameras of the GONG network were upgraded to 1024 × 1024 square pixels. During

Table 3
Rank Correlation, ρ for m-averaged Mean Mode Parameters for Solar Cycles 23 and 24 and All Data

Cycle No.	Frequency (ν)		Amplitude (A)		Width (Γ)	
	Original	Corrected	Original	Corrected	Original	Corrected
23	0.91	0.91	−0.64	−0.72	0.68	0.81
24	0.88	0.90	−0.45	−0.93	0.38	0.81
All Data	0.89	0.89	−0.58	−0.67	0.56	0.76

Note. The significance, p, in each case is less than 10^{-6}.

this process, the observations were interrupted and as a result the network recorded some of the lowest duty cycles (see Figure 1). Kiefer et al. removed this artifact by matching the parameters on either side of the jump using a correction factor that is dependent on the frequency and the harmonic degree of the mode since the jumps were found to be dependent on these factors. However, we only notice the jump in uncorrected mode amplitudes during GM 60 (visible in the top left panel of Figure 14) and none around GM 100, probably because the mode amplitudes plotted here are averaged over all the frequencies and harmonic degrees and not over different ranges. Furthermore, this jump is not visible in the corrected mode amplitudes (red points and the associated curve), confirming that the effect is due to the observed low duty cycle.

4.3. Comparison between Cycles 23 and 24

It is now well known that the minimum between solar cycles 23 and 24 was unusually deep and long, and cycle 24 is relatively weaker than cycle 23 (Jain et al. 2016; Broomhall 2017; Howe et al. 2017; Tapping & Morgan 2017). As a result, this provides a unique opportunity to compare the variation of the oscillation-mode parameters between two very distinct solar activity cycles. Using GOLF data, Salabert et al. (2015) demonstrated that the frequencies of high-frequency modes varied by 30% less in the rising phase of cycle 24 than in cycle 23, which agrees with the surface measurements of the Sun's magnetic activity. In a similar investigation, based on BISON data, Basu et al. (2012) also inferred that the frequencies of low-degree p-modes higher than 2450 μHz behaved in a similar manner in cycles 22, 23, and the rising phase of cycle 24. In contrast, the frequencies of the low-frequency modes appear to change by the same amount, implying that the magnetic field below 1400 km is unchanged between these two cycles. In a later investigation, Broomhall & Nakariakov (2015) compared low-degree helioseismic frequencies with several different proxies of the solar activity and reported interesting differences between cycles 23 and 24. For example, in cycle 24 the deviation decreases between the solar proxies and oscillation frequencies, while it increases between interplanetary proxies and frequencies. However, the properties of quasi-biennial oscillations remain approximately similar in both cycles. Based on this study, the authors suggest that the oscillation frequencies behave differently in even and odd solar cycles. Recently, Jain et al. (2018) analyzed sun-as-a-star observations from different instruments spanning over cycles 22–24 and suggest that the structural and magnetic changes responsible for modifying the frequencies remained comparable between cycle 23 and cycle 24, but differ from cycle 22, supporting the idea of Basu et al. (2012) that the magnetic layer of the Sun has become thinner since the beginning of cycle 23 and has continued during cycle 24. This argument was further supported by Howe et al. (2018),who utilized data from Big Bear Solar Observatory, GONG, MDI, and HMI to examine the shifts in medium-degree mode frequencies and their sensitivity to solar activity levels in the last three cycles. They found small but significant systematic differences between the cycles, with solar cycle 24 showing a frequency shift about 10% larger than that of cycle 23 for the same change in activity as determined by the 10.7 cm radio flux.

Here, we briefly discuss the variations between cycle 23 and 24 by comparing the rank correlation coefficients between the m-averaged mean mode parameters and $F_{10.7}$. For this, we split the data at the reference GONG month, which marks the solar minimum period between cycles 23 and 24. Thus, cycle 23 covers the period 1996 May 1 through 2009 January 16 and consists of 127 sets (as we have neglected few data sets that cover the cycle 22), while cycle 24 consists of the remaining period with 100 sets of data. The Spearman's rank correlation, with the two-sided significance for the mean frequencies, widths, and amplitudes, are tabulated in Table 3. It is clear that the corrected mode frequencies and widths have similar correlations during both the cycles, although cycle 23 is stronger than cycle 24. However, for mode amplitudes, we find higher anti-correlation during cycle 24, indicating a better alignment with the radio flux. It is possible that the observed power has not reached the minimum level yet, because we only have partial data for cycle 24 and this is reflected in the higher correlation coefficient as compared to cycle 23. In the domain of low-degree modes, Broomhall et al. (2015) reported a drop in powers observed in cycle 24 below the value predicted by the linear regression between $F_{10.7}$ and the power, and speculated that this deviation could be related to the change in the magnitude of the frequency shifts observed in low-frequency modes between cycles 22 and 23 (Basu et al. 2012) or due to the imprecise fitting of the asymmetry associated with the amplitude. It is also interesting to note that when all the data are used, the correlation is weaker by about 6% as compared to using individual cycles. All these salient features related to solar cycles warrant a more detailed investigation, but this is beyond the scope of the present paper.

4.4. Correlation of Individual Modes

In this section, we focus on the individual modes instead of mean quantities and investigate their correlation with $F_{10.7}$ as a function of frequency. The rank correlation coefficients for frequency (bottom panel), amplitudes (middle panel) and widths (top panel) as a function of frequency are shown in Figure 15. We find that the frequency correlation maximizes in the 3500–4500 μHz range, while the amplitude and width correlation peak in the 3000–3500 μHz range. Since the mode parameters are best measured in the 3 mHz range, it is surprising that the correlation between the mode frequencies

Table 4
Rank Correlation, ρ, and Its Significance p, for m-averaged Mean Mode Parameters

Frequency Range (μHz)	Number of Modes	Frequency (ν)		Amplitude (A)		Width (Γ)	
		ρ	p	ρ	p	ρ	p
1500–2000	286	0.36	0	−0.53	0	0.45	$<10^{-12}$
2000–2500	319	0.61	0	−0.68	0	0.57	0
2500–3000	314	0.62	0	−0.91	0	0.77	0
3000–3500	329	0.75	0	−0.91	0	0.86	0
3500–4000	344	0.85	0	−0.26	5.9×10^{-5}	0.66	0
4000–4500	310	0.54	0	0.38	1.6×10^{-9}	−0.16	0.01
1500–3500	1248	0.74	0	−0.85	0	0.77	0
1500–4500	1902	0.89	0	−0.67	0	0.76	0

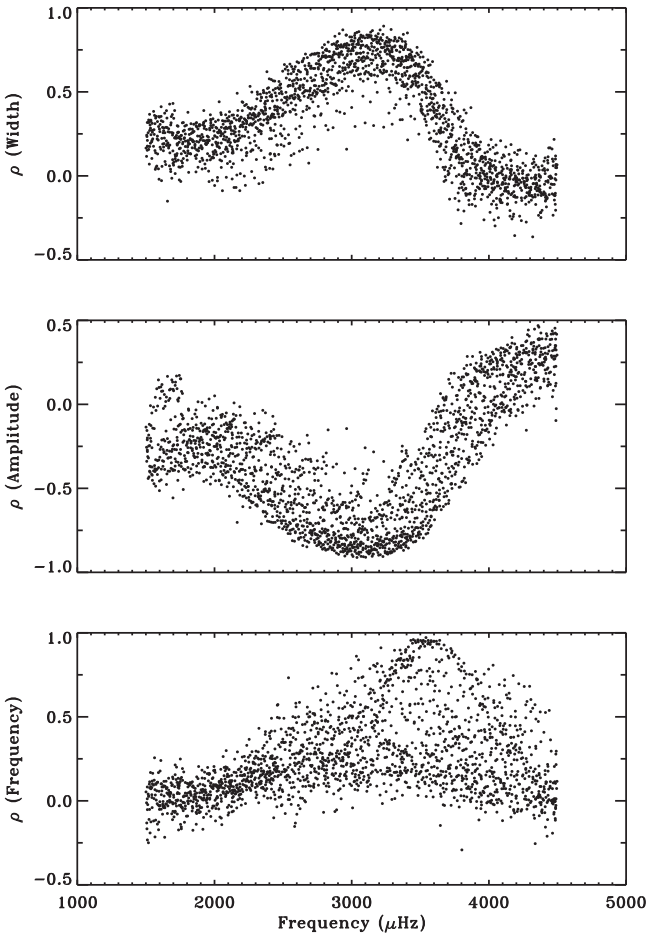

Figure 15. Spearman's rank correlation coefficient, ρ, between corrected mode parameters and $F_{10.7}$ for all modes common in the 237 GONG data sets. The bottom panel is for frequency shifts, the middle panel is for normalized amplitudes, and the top panel is for normalized widths.

and solar activity does not peak in this range. In order to interpret this behavior, we examine the mode parameters in bins of 500 μHz and recalculate the Spearman's rank correlation for each mode parameter. Table 4 displays the results along with the number of modes in that range. For completeness, we also tabulate the findings in the frequency range of 1500–3500 μHz and 1500–4500 μHz. Clearly, the m-averaged frequencies in the 3500–4000 μHz band have a 12% higher correlation than the 3000–3500 μHz band, which agrees with the result that the activity-related correlation increases with increasing frequencies (Howe et al. 2018; K. Jain et al. 2019, in preparation). This could also be related to the fact that the magnitudes of the frequency shifts at higher frequencies are larger and therefore any random errors in the data will have a smaller impact on the correlation.

Table 4 further illustrates that the value of ρ for mode amplitudes and widths varies a lot with different frequency ranges. In case of mode amplitudes, ρ is nearly equal in 2500–3000 μHz and 3000–3500 μHz bands and agrees with the values reported in Kiefer et al. (2018). However, in other bands, these authors report a higher value, which could be due to their analysis method, which included only independent data sets. Surprisingly, for the widths, our values are higher than those reported in Kiefer et al. (2018) in all frequency bands and we cannot provide any possible explanation. Finally, we note that at the highest frequency range, the correlation coefficients change sign, the amplitude is in phase, while the widths are in anti-phase and could be related to the depth where these modes propagate. However, the significance associated with the correlation of widths is very small, indicating that the calculated coefficient is unreliable. In addition, we must also consider the possibility that in these high-frequency ranges, the asymmetry parameter may play an important role and the deviation may be due to the inaccurate determination of the mode parameters, as the GONG pipeline fits a symmetric profile to the observed power spectrum. Such opposite behavior was earlier pointed out in the study of oscillation frequencies at the low ($\nu \leqslant 1700$ μHz) and high ($\nu \geqslant 4200$ μHz) ends of the frequency range, and was then attributed to the lack of sufficient modes at these ν ranges (Tripathy et al. 2007, and references therein).

5. Conclusion

In this paper, we have investigated the effect of the window function on the mode parameters by analyzing simulated data generated from a base set by changing the window functions. The new window functions were randomly chosen from real observations. Since the mode parameters are known to vary with the solar cycle, the base time series was chosen during the minimum activity period. The investigation confirms earlier results of low-degree modes (Chaplin et al. 2004) that the effect of the duty cycle on the mode frequencies is not significant. However, mode amplitudes and widths are significantly affected by the duty cycle. Using the corrected mode parameters, we then analyzed 22 yr of standard GONG data for activity-related changes and found that the widths follow the phase of the cycle, i.e., the modes are heavily damped during the solar maximum. On the other hand, the mode amplitudes are anti-correlated with solar activity, decreasing as solar activity increases. These findings corroborate the results

of Kiefer et al. (2018), although the analysis methods are not identical. However, both studies use a single activity index, $F_{10.7}$, as a proxy of the activity, which is not a direct measure of the magnetic properties of the Sun. Thus, it is desirable to carry out a similar study using a magnetic field indicator. We further analyze the mode parameters for the two solar cycles 23 and 24 separately and find some interesting differences, e.g., we note that the mode amplitudes have a higher rank correlation in cycle 24 compared to cycle 23, although cycle 23 is stronger than cycle 24, while the mode frequencies and widths follow the conventional wisdom that the high activity period is associated with higher frequencies and widths. Nonetheless, a precise comparison between the two cycles can only be carried out when data for the entiretry of cycle 24 are available. Correlation of individual modes with $F_{10.7}$ also demonstrated that the value of ρ varies significantly between different frequency bands. In the highest frequency bands between $4000 \leqslant \nu \leqslant 4500$, we also found that ρ changed sign, i.e., the mode amplitude is in phase with the activity cycle, while the width is in anti-phase, indicating a frequency dependence similar to the mode frequencies. This needs to be investigated further. Finally, we note that a similar regression analysis should be carried out for MDI and HMI data, which have smaller and different gap structures compared to the GONG data.

This work was partially carried out through the National Solar Observatory Research Experiences for Undergraduates (REU) Program, which is funded by the National Science Foundation (NSF) through Award No. 1659878. We thank the anonymous reviewer for the comments, which helped to improve the paper. The National Solar Observatory is operated by the Association of Universities for Research in Astronomy, Inc. (AURA) under cooperative agreement with the NSF. This work utilizes GONG data obtained by the NSO Integrated Synoptic Program (NISP), managed by the National Solar Observatory, the Association of Universities for Research in Astronomy (AURA), Inc. under a cooperative agreement with the National Science Foundation. The data were acquired by instruments operated by the Big Bear Solar Observatory, High Altitude Observatory, Learmonth Solar Observatory, Udaipur Solar Observatory, Instituto de Astrofísica de Canarias, and Cerro Tololo Interamerican Observatory.

ORCID iDs

S. C. Tripathy https://orcid.org/0000-0002-4995-6180
K. Jain https://orcid.org/0000-0002-1905-1639

References

Anderson, E. R., Duvall, T. L., Jr., & Jefferies, S. M. 1990, ApJ, 364, 699
Basu, S., Broomhall, A.-M., Chaplin, W. J., & Elsworth, Y. 2012, ApJ, 758, 43
Broomhall, A.-M. 2017, SoPh, 292, 67
Broomhall, A.-M., & Nakariakov, V. M. 2015, SoPh, 290, 3095
Broomhall, A.-M., Pugh, C. E., & Nakariakov, V. M. 2015, AdSpR, 56, 2706
Brown, T. M., & Christensen-Dalsgaard, J. 1990, ApJ, 349, 667
Chang, H.-Y., & Gough, D. 1995, in ESA Special Publication 376, 4th Soho Workshop, ed. J. T. Hoeksema et al. (Paris: ESA), 179
Chaplin, W. J., Elsworth, Y., Isaak, G. R., et al. 2003, A&A, 398, 305
Chaplin, W. J., Elsworth, Y., Isaak, G. R., et al. 2004, A&A, 424, 301
Fahlman, G. G., & Ulrych, T. J. 1982, MNRAS, 199, 53
Harvey, J. W., Hill, F., Hubbard, R. P., et al. 1996, Sci, 272, 1284
Hill, F., Ambastha, A., Ball, W., et al. 1988, in ESA Special Publication 286, Symp. on Seismology of the Sun and Sun-Like Stars, ed. E. J. Rolfe (Paris: ESA), 209
Hill, F., Anderson, E., Howe, R., et al. 1998, in ESA Special Publication 418, SOHO 6/GONG 98 Workshop, ed. S. Korzennik (Paris: ESA), 231
Howe, R., Chaplin, W. J., Davies, G. R., et al. 2018, MNRAS, 480, L79
Howe, R., Davies, G. R., Chaplin, W. J., et al. 2017, MNRAS, 470, 1935
Jain, K., Tripathy, S., Hill, F., et al. 2018, in IAU Symp. 340, Long-term Datasets for the Understanding of Solar and Stellar Magnetic Cycles, ed. D. Banerjee (Cambridge: Cambridge Univ. Press), 27
Jain, K., Tripathy, S., Simoniello, R., & Hill, F. 2016, AAS Solar Physics Division Meeting, 47, 7.16
Jain, K., Tripathy, S. C., & Hill, F. 2009, ApJ, 695, 1567
Jain, K., Tripathy, S. C., & Hill, F. 2011, ApJ, 739, 6
Kiefer, R., Komm, R., Hill, F., Broomhall, A.-M., & Roth, M. 2018, SoPh, 293, 151
Komm, R. W., Gu, Y., Hill, F., Stark, P. B., & Fodor, I. K. 1999, ApJ, 519, 407
Komm, R. W., Howe, R., & Hill, F. 2000, ApJ, 531, 1094
Lazrek, M., & Hill, F. 1993, A&A, 280, 704
Salabert, D., García, R. A., Pallé, P. L., & Jiménez-Reyes, S. J. 2009, A&A, 504, L1
Salabert, D., García, R. A., & Turck-Chièze, S. 2015, A&A, 578, A137
Simoniello, R., Jain, K., Tripathy, S. C., et al. 2013, ApJ, 765, 100
Tapping, K., & Morgan, C. 2017, SoPh, 292, 73
Tripathy, S. C., Bogart, R., & Jain, K. 2018, in Proc. SDO Workshop, Catalyzing Solar Connections (Washington, DC: NASA), 56
Tripathy, S. C., Hill, F., Jain, K., & Leibacher, J. W. 2006, in ESA Special Publication 624, SOHO 18/GONG 2006/HELAS I, ed. K. Fletcher & M. Thompson (Paris: ESA), 93
Tripathy, S. C., Hill, F., Jain, K., & Leibacher, J. W. 2007, SoPh, 243, 105
Tripathy, S. C., Jain, K., & Hill, F. 2015, ApJ, 812, 20
Tripathy, S. C., Jain, K., Hill, F., & Leibacher, J. W. 2010, ApJL, 711, L84